



# Cu Electrodeposition on Nanostructured MoS<sub>2</sub> and WS<sub>2</sub> and Implications for HER Active Site Determination

Longfei Wu,<sup>1,a</sup> Nelson Y. Dzade,<sup>2,3</sup> Ning Chen,<sup>4</sup> Bas van Dijk,<sup>5</sup> Shashank Balasubramanyam,<sup>6</sup> Akhil Sharma,<sup>6</sup> Lu Gao,<sup>1</sup> Dennis G. H. Hetterscheid,<sup>5</sup> Emiel J. M. Hensen,<sup>1</sup> Ageeth A. Bol,<sup>6</sup> Nora H. De Leeuw,<sup>2,7</sup> and Jan P. Hofmann<sup>1,8,z</sup>

<sup>1</sup>Laboratory for Inorganic Materials and Catalysis, Department of Chemical Engineering and Chemistry, Eindhoven University of Technology, 5600 MB Eindhoven, The Netherlands

<sup>2</sup>Faculty of Geosciences, Utrecht University, 3508 TA Utrecht, The Netherlands

<sup>3</sup>School of Chemistry, Cardiff University, CF10 3AT, Cardiff, United Kingdom

<sup>4</sup>Hard X-ray MicroAnalysis (HXMA) BL, Canadian Light Source, University of Saskatchewan, Saskatoon, SK, S7N 2V3, Canada

<sup>5</sup>Leiden Institute of Chemistry, Leiden University, 2333 CC Leiden, The Netherlands

<sup>6</sup>Department of Applied Physics, Eindhoven University of Technology, 5600 MB Eindhoven, The Netherlands

<sup>7</sup>School of Chemistry, University of Leeds, Leeds LS2 9JT, United Kingdom

<sup>8</sup>Surface Science Laboratory, Department of Materials and Earth Sciences, Technical University of Darmstadt, 64287 Darmstadt, Germany

Cu electrodeposition in both underpotential and overpotential regimes on nanostructured MoS<sub>2</sub> and WS<sub>2</sub> prepared by plasma-enhanced atomic layer deposition has been studied in detail. A combination of electrochemical methods, advanced characterization by X-ray absorption spectroscopy (XAS) as well as theoretical modelling were employed to reveal Cu adsorption modes on transition metal dichalcogenides (TMDs) from initial stages until bulk deposition. Since Cu UPD on TMDs has been used recently to evaluate the number of electrochemically active sites ( $N_{AS}$ ) for H<sub>2</sub> evolution reaction, we evaluate and discuss here the implications of the Cu electrodeposition phenomena on nanostructured MoS<sub>2</sub> and WS<sub>2</sub> gauging the general applicability of the Cu UPD method for number of HER active sites determination in TMDs. Although an apparently better correlation of HER current density with Cu UPD charge than with double layer capacitance is found, the Cu UPD method cannot be used quantitatively because of the absence of a clear H UPD phenomenon on the studied nanostructured TMDs. This is in contrast to platinum group metal catalysts where H UPD and Cu UPD sites are strongly correlated.

© 2020 The Author(s). Published on behalf of The Electrochemical Society by IOP Publishing Limited. This is an open access article distributed under the terms of the Creative Commons Attribution 4.0 License (CC BY, <http://creativecommons.org/licenses/by/4.0/>), which permits unrestricted reuse of the work in any medium, provided the original work is properly cited. [DOI: 10.1149/1945-7111/aba5d8]



Manuscript submitted June 10, 2020; revised manuscript received July 4, 2020. Published July 23, 2020. *This paper is part of the JES Focus Issue on 2D Layered Materials: From Fundamental Science to Applications.*

Supplementary material for this article is available [online](#)

Underpotential deposition (UPD) refers to electrochemical deposition of metal atoms at potentials more positive than those required for bulk deposition.<sup>1</sup> Typically, UPD is driven by the work function differences between two metals that a less noble metal is deposited on a more noble metal substrate at potentials above the reversible potential ( $E_{Me^{z+}/Me^0}$ ). The adsorption and deposition of metal atoms in full or incomplete monolayers alter the structural, optical and electronic properties of the substrate profoundly. Thus, the UPD method has been broadly used for tuning activity and selectivity of catalysts, identifying of crystallographic facets, protecting catalysts from corrosion, determining trace metals, nanoparticle shape control, as well as surface area measurement determination.<sup>2–7</sup> It is particularly convenient in determining the number of active sites ( $N_{AS}$ ) for noble metal electrodes or noble metal particles loaded on inert supports.<sup>8,9</sup> For instance, Green et al. reported that both surface area and surface composition of Pt-Ru electrocatalyst could be determined by Cu UPD.<sup>8</sup> Although precious metals such as Pt or Ru exhibit high activities for the hydrogen evolution reaction (HER), the scarcity and high cost of these elements have motivated the search for Earth-abundant metal-based catalysts with comparably high activities and stabilities. Recent advances in materials science and nanotechnology have demonstrated the significant potential of transition metal dichalcogenides (TMDs) such as MoS<sub>2</sub> and WS<sub>2</sub> as promising alternatives to Pt in catalyzing the HER.<sup>10</sup> A variety of novel methodologies, e.g.

nano-structuring and defect engineering, have been reported to fabricate TMD-based HER catalysts.<sup>11–13</sup> However, comparison of experimental data from different laboratories or preparation methods is problematic without a proper normalization of the actual electrochemically active surface area (ECSA) or the number of active sites ( $N_{AS}$ ) of the different catalyst samples.<sup>1</sup> Specific ex situ and in situ methods have been reported for different electrode materials, each with their own limitations.<sup>1</sup> Correlations between the surface area determined by gas physisorption methods, such as the BET (Brunauer–Emmett–Teller) method, and the ECSA are typically poor.<sup>14</sup> Hydrogen, oxygen, and CO adsorption are well known in situ electrochemical methods for determining  $N_{AS}$ . Yet, these methods are limited in scope to only a few noble metals that show high affinity to these probe molecules. The electrochemical double layer capacitance (DLC), which is obtained from measurements in a potential region, where electric double layer charging is the only electrochemical process, offers a versatile alternative for estimating ECSA of compound electrocatalysts, such as sulfides, carbides and phosphides.<sup>12,15–17</sup> However, a major challenge for this method is that it depends on the availability of a reliable value for the specific capacity per unit area.<sup>18–20</sup> Furthermore, this method does not provide any information about  $N_{AS}$  which is needed to determine the intrinsic activity of the catalyst under investigation.

Recently, UPD of Cu on metal chalcogenides (e.g. CdS, WS<sub>2</sub>, Pd<sub>3</sub>P<sub>2</sub>S<sub>8</sub>) has been reported and employed to access the number of electrochemically active sites.<sup>21–24</sup> However, further studies are required to investigate the UPD adlayer formation and to correlate it with the actual nature and number of catalytically active sites. Therefore, we investigate here in detail the electrodeposition phenomena of Cu on nanostructured MoS<sub>2</sub> and WS<sub>2</sub> to get insight into the Cu adsorption modes and the transition between UDP and

<sup>a</sup>Present Address: Debye Institute for Nanomaterials Science, Inorganic Chemistry and Catalysis, Faculty of Science, Utrecht University, Universiteitsweg 99, 3584 CG Utrecht, The Netherlands.

<sup>z</sup>E-mail: [hofmann@surface.tu-darmstadt.de](mailto:hofmann@surface.tu-darmstadt.de)

overpotential deposition (OPD) regimes by employing electrochemical and spectroscopic methods as well as theoretical modeling. Then, we evaluate the correlation between HER activity and Cu UPD to check how far the Cu UPD method is quantitative on TMDs towards  $N_{AS}$  determination. Since, in contrast to Pt-group metals, no clear hydrogen UPD feature is present on the studied TMDs, we find it ambiguous to correlate the hydrogen adsorption sites with Cu UPD sites. Despite the apparent linear relationship between HER activity and Cu UPD charge, we indicate that Cu UPD cannot be generally employed as a quantitative method for determination of  $N_{AS}$  on TMDs.

## Experimental

**Preparation of nanostructured TMDs.**—MoS<sub>2</sub> and WS<sub>2</sub> films were prepared by plasma-enhanced atomic layer deposition (PEALD) in an Oxford Instrument FlexALTM ALD reactor on either electrochemical quartz crystal microbalance (EQCM) gold electrodes or glassy carbon electrodes (Carbon-Vitreous-3000C-Foil-VC000550, Goodfellow Cambridge Ltd. UK).<sup>24,25</sup> The PEALD process was based on a combination of a metal organic precursor bis(tert-butylimido) bis(dimethylamido) molybdenum ( $[(N^tBu)_2(NMe_2)_2Mo]$ ) or  $[(N^tBu)_2(NMe_2)_2W]$  and H<sub>2</sub>S + Ar or H<sub>2</sub>S + H<sub>2</sub> + Ar plasma as a co-reactant.<sup>24,25</sup> WS<sub>2</sub> and MoS<sub>2</sub> films with different morphologies and number of ALD cycles, i.e. different thicknesses, are tested in this work.

**Electrochemical characterization.**—Electrochemical characterization was performed in a three-electrode configuration cell with MoS<sub>2</sub> or WS<sub>2</sub> deposited glassy carbon plates (22 × 22 × 2 mm<sup>3</sup>) as the working electrode, Pt foil as the counter electrode (Pt contamination under the same conditions was excluded by XPS measurements in our previous research<sup>26</sup>) and a saturated calomel electrode (SCE, calibrated with a value of +0.269 V vs reversible hydrogen electrode (RHE)) as the reference electrode. Hydrogen evolution measurements were carried out in an Ar-saturated 0.1 M H<sub>2</sub>SO<sub>4</sub> solution and Cu UPD was performed in an Ar-saturated 2 mM CuSO<sub>4</sub> in 0.1 M H<sub>2</sub>SO<sub>4</sub>.

**X-ray absorption spectroscopy (XAS).**—XAS was performed at the 061D-1 (HXMA) beamline of the Canadian Light Source (CLS). Samples were mounted in an N<sub>2</sub> protected holder and measured at a grazing incidence angle of 0.2° in fluorescence detection mode by using a 32 element Canberra array detector. X-ray Near Edge Spectroscopy (XANES) and Extended X-ray Absorption Fine Structure (EXAFS) spectroscopy were collected at the Cu K-edge (8.98 keV) and recorded by co-addition of 5 scans. The code used for XANES modeling was FDMNES.<sup>27</sup> The structural model for metallic Cu was obtained from Crystallography Open Database (COD ID: 1512504).<sup>28</sup> Structural models of Cu bonding on MoS<sub>2</sub> were obtained from DFT calculations, which are discussed in detail in Part V of the SI.

**Density functional theory (DFT) calculations.**—DFT calculations were carried out using the Vienna Ab-initio Simulation Package (VASP), a periodic plane wave DFT code which includes the interactions between the core and valence electrons via the Projector Augmented Wave (PAW) method.<sup>29–31</sup> The generalized gradient approximation (GGA) with the Perdew–Burke–Ernzerhof (PBE) functional was used for the calculation of the electronic exchange–correlation potential.<sup>32</sup> Wave functions were expanded in a plane wave basis with a high energy cutoff of 600 eV and the convergence criterion was set to 10<sup>−6</sup> eV between two ionic steps for the self-consistency process. The long-range Van der Waals interactions were incorporated in the DFT calculations through the DFT-D3 scheme by Grimme, which adds a semi-empirical dispersion potential to the conventional Kohn–Sham DFT energy.<sup>33</sup>

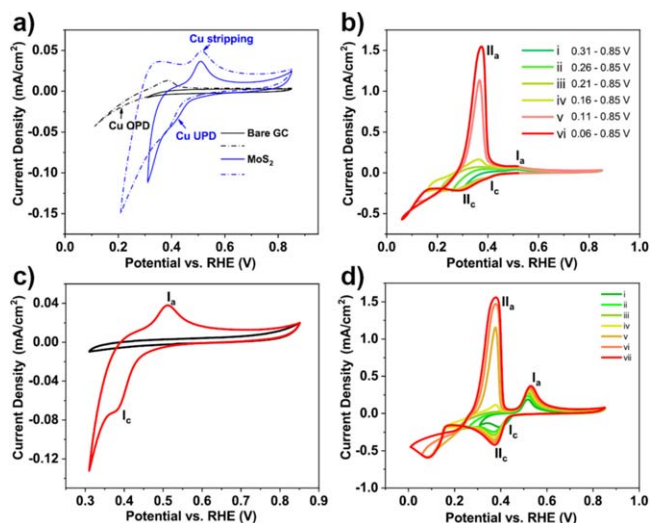


**Figure 1.** (a) Cyclic voltammetry (CV) curves of bare glassy carbon substrate (black curves) and MoS<sub>2</sub> on glassy carbon (blue curves) in 2 mM CuSO<sub>4</sub> in 0.1 M H<sub>2</sub>SO<sub>4</sub> with different potential range 0.0–0.86 V vs RHE, scan rate: 50 mV s<sup>−1</sup>; (b) CV curves of nanostructured MoS<sub>2</sub> in 2 mM CuSO<sub>4</sub> in 0.1 M H<sub>2</sub>SO<sub>4</sub> with gradually increased potential scan range; (c) CV curves of MoS<sub>2</sub> on glassy carbon in 0.1 M H<sub>2</sub>SO<sub>4</sub> (black curve) and 2 mM CuSO<sub>4</sub> in 0.1 M H<sub>2</sub>SO<sub>4</sub> (red curve), scan rate: 50 mV s<sup>−1</sup>; (d) CV curves of WS<sub>2</sub> film in 2 mM CuSO<sub>4</sub> in 0.1 M H<sub>2</sub>SO<sub>4</sub> with potential range 0.0–0.86 V vs RHE. Scan rate: 50 mV s<sup>−1</sup>.

## Results and Discussions

**Cu UPD on TMDs.**—Figure 1 displays the potential dynamic profiles of different MoS<sub>2</sub> films during Cu UPD and overpotential deposition (OPD). For comparison, cyclic voltammetry (CV) curves of both the bare glassy carbon (GC) substrate and MoS<sub>2</sub> film are given in Fig. 1a. From these data, we can conclude that the cathodic reduction of Cu<sup>2+</sup> on MoS<sub>2</sub> starts at more positive potentials than bulk Cu deposition on bare GC. The Nernst potential of  $E_{Cu^{2+}/Cu}$  in this system (2 mM CuSO<sub>4</sub>) is +0.26 V vs RHE while the UPD on MoS<sub>2</sub> shifts around +100 mV. A series of cyclic voltammograms with varying potential scan ranges were recorded (Fig. 1b). The data in Fig. 1 show the transition from Cu UPD to OPD with decreasing deposition potential. The complex loop between 0 and 0.2 V vs RHE as shown in Fig. 1b might be due to intercalation of Cu, which is reported in previous work.<sup>34,35</sup> The same phenomenon is also observed for WS<sub>2</sub> (Fig. 1d). Thus, Cu can be deposited on MoS<sub>2</sub> and WS<sub>2</sub> at potentials more positive than the Nernstian potential, or in other words Cu UPD occurs on MoS<sub>2</sub> and WS<sub>2</sub>.

**Electrochemical quartz crystal microbalance (EQCM) measurements.**—To study the UPD phenomenon of Cu atoms on MoS<sub>2</sub> surfaces in more detail, we employed electrochemical quartz crystal microbalance (EQCM) measurements to quantitatively analyze the mass change during the Cu UPD process.<sup>36</sup> Figure 2 presents cyclic voltammograms (CV) and the simultaneously recorded frequency change ( $\Delta f$ ) on PE-ALD prepared MoS<sub>2</sub>-Au-EQCM electrodes in 2 mM CuSO<sub>4</sub> in 0.1 M H<sub>2</sub>SO<sub>4</sub>. Upon negative scanning from +0.85 V, the QCM frequency first remains constant and then decreases quickly as the first Cu UPD peak appears at  $\sim$ +0.40 V. On the reverse scan, the frequency gradually increases accordingly when the Cu stripping peak approaches  $\sim$ +0.50 V. Although there might be drifts in EQCM, the Cu UPD and stripping peaks increase gradually within the first four CV scans and remain similar for the 5th and 6th scan, which is also reflected in the frequency change in EQCM measurements. In addition, the starting frequency ( $\sim$ 0.8 V vs RHE) value becomes larger with increasing scan numbers and remains constant after the 4th scan. This phenomenon can be

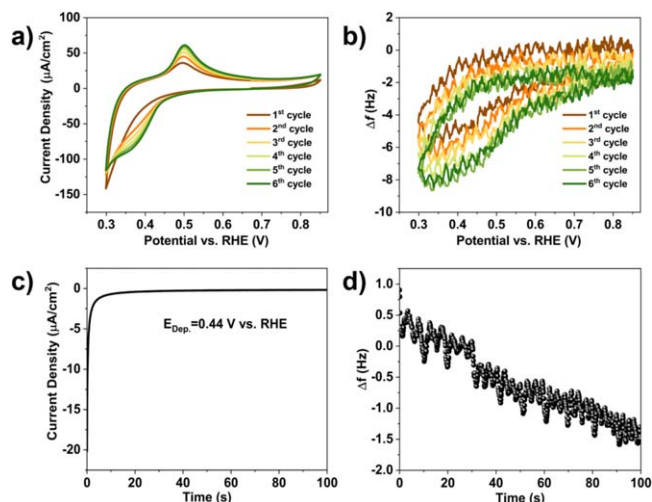


**Figure 2.** Cyclic voltammetry (CV) (a) and simultaneously recorded frequency change (b) on MoS<sub>2</sub> deposited on a polycrystalline Au-EQCM electrode (400 ALD cycles, OoPo structure, Table SIII) in 2 mM CuSO<sub>4</sub> in 0.1 M H<sub>2</sub>SO<sub>4</sub>. Scan rate: 50 mV s<sup>-1</sup>. (c) Current density curve (c) of Cu UPD at 0.44 V vs RHE for 100 s and the corresponding frequency change (d).

ascribed to the strong binding between Cu atoms and MoS<sub>2</sub> leading to an incomplete desorption of adsorbed Cu in the initial cycles. However, the absolute frequency change in each cycle (Fig. 2b) remains constant, which suggests that the same amount of Cu has adsorbed. The frequency change ( $\Delta f$ ) in EQCM is proportional to the change in mass ( $\Delta m$ ) per unit area ( $A$ ) on the working electrode, given by the Sauerbrey equation:

$$\Delta f = -(2f_0^2) \Delta m / A \sqrt{\mu_q \rho_q}$$

where  $f_0$  is the resonance frequency (Hz),  $A$  is the piezo-electrically active crystal area,  $\mu_q$  is the shear modulus of quartz ( $2.947 \times 10^{11} \text{ g} \cdot \text{cm}^{-1} \cdot \text{s}^{-2}$ ) and  $\rho_q$  is the density of quartz ( $2.648 \text{ g cm}^{-3}$ ).<sup>36–39</sup> Based on this equation, the sensitivity of the EQCM is calculated to be  $13 \text{ ng} \cdot \text{Hz}^{-1} \cdot \text{cm}^{-2}$ . Therefore, the adsorbed Cu atoms on the MoS<sub>2</sub> electrode amount to  $78 \pm 7 \text{ ng} \cdot \text{cm}^{-2}$  or  $7.3 \pm 0.6 \times 10^{14} \text{ atoms} \cdot \text{cm}^{-2}$  in the range of +0.31 to +0.85 V vs RHE. Figure 2c, d displays the current density and corresponding frequency change at Cu UPD potential (0.44 V vs RHE) for 100 s. Given the 2-electron process for Cu UPD, the charge calculated via EQCM is  $78 \sim \mu\text{C cm}^{-2}$ , which is higher than that obtained by integrating the current density over time ( $45 \sim \mu\text{C cm}^{-2}$ ). The Cu UPD charge discrepancy between EQCM and recorded current density can be ascribed to the poor conductivity and hydrophobic effects of semiconducting MoS<sub>2</sub> that result in significant deviations of  $\Delta f$ , which greatly lower the sensitivity of EQCM measurements.<sup>40</sup> In conjunction with electrochemical measurements, XAS measurements were also performed to enable the assignment of structural configurations for Cu deposition on TMDs.

**XAS analysis.**—Grazing incidence X-ray absorption spectroscopy (XAS) at the Cu K-edge, including X-ray absorption near-edge structure (XANES) and extended X-ray absorption fine structure (EXAFS), allows for the investigation of the local structural environment and the site occupancy of adsorbed Cu on TMDs.<sup>41,42</sup> As shown in Fig. 3, the similarity in the line shape between the sample of Cu deposition at 0.21 V vs RHE and Cu foil for the XANES edge jump within region “A” suggests that likely there is a Cu species with Cu-Cu direct bonding present in the measured sample. In addition, the clearly resolved edge shift by  $\sim 2 \text{ eV}$  (region “B” indicated by the arrow, Fig. 3a) indicates that there exists a second, different Cu species without Cu-Cu direct

bonding, which may correspond to Cu atoms directly adsorbed on MoS<sub>2</sub>. The theoretically modeled Cu adsorbate system reveals a particle-size induced progressive change in the XANES features (Fig. 3b) for metallic Cu. The smallest particle used for the modeling is a cluster R3.0 Å (cluster size 3.0 Å), containing 12 Cu atoms. Figure 3c compares the sample spectrum and the XANES theoretical modeling based on a R3.0 Å cluster. The similarity in XANES between the two extends from the edge jump up to the white line (A1). In addition, the metallic Cu specific shoulder feature “C” is revealed for the measured sample and the theoretical model at around the same energy position, further suggesting a Cu-Cu direct bonding. Nevertheless, the edge shift in Fig. 3a is also well pronounced comparing with R3.0 Å, confirming the presence of Cu adsorption on MoS<sub>2</sub>. Thus, although the Cu deposition potential (0.21 V vs RHE) is slightly negative than UPD condition, XANES based observation suggests two coexisting Cu species in the sample, i.e., metallic Cu-Cu direct bonding, and Cu atoms adsorbed on MoS<sub>2</sub>.

Using density functional theory (DFT) calculations, we evaluated possible Cu bonding scenarios on MoS<sub>2</sub>, namely single Cu monodentate (M1, Fig. 4a), single Cu bidentate (M2, Fig. 4b) and paired Cu monodentate (M3, Fig. 4c) configurations. Fig. 4c presents the comparison of experimental and FEFF (automated program for ab initio multiple scattering calculations of XAS) modeled EXAFS magnitudes of Fourier Transforms (FT), which indicates the existence of M2 and M3 species upon Cu deposition at +0.21 V on MoS<sub>2</sub>, with bond distances of 2.36 Å for Cu-S (M2) and 2.56 Å for Cu-Cu (M3) (Table SIV is available online at [stacks.iop.org/JES/167/116517/mmedia](https://stacks.iop.org/JES/167/116517/mmedia)).<sup>27</sup> As the Cu-K edge XAS was recorded for a sample with Cu deposition at a relatively negative potential ( $< +0.26 \text{ V}$  vs RHE), it is reasonable to assume the existence of Cu-Cu direct bonding, indicating the presence of Cu-Cu, which is consistent with XANES analysis shown in Fig. 3. Although the sample was characterized under more negative potentials than Cu UPD, the strong contribution of the Cu bidentate (M2) configuration in the R-space of the Fourier Transformed EXAFS (Figs. 4d, 4e) indicates the bonding mode of Cu UPD on MoS<sub>2</sub>, which is also indicated by the edge shift in XANES (Fig. 3). It should be noted that the current EXAFS fitting models are based on Cu adsorption on MoS<sub>2</sub> basal planes. Even though edge sites of TMDs have been identified to be the HER active sites, FEFF modelled XANES of adsorbed Cu on MoS<sub>2</sub> edges (Fig. S16) did not fit well with the experimental data.<sup>43</sup> However, DFT derived optimized structures of Cu on S-Mo-S edges (Fig. S15) indicates that Cu-bridge-S, which is structurally similar to bidentate binuclear M2 (Fig. 4b), has the largest (negative) average binding energy ( $E_{\text{ab}}$ ), which points to the adsorption of Cu atoms on edge or defect sites.<sup>44</sup> Owing to the ultrathin, sub-monolayer nature of the Cu UPD layers on the MoS<sub>2</sub> and WS<sub>2</sub> samples, the S/N ratio of the data recorded for Cu UPD sample (Cu\_MoS<sub>2</sub>@0.44 V) did not allow us to unambiguously prove the absence of Cu-Cu direct bonding (Fig. S11). Despite that, we think it is meaningful to show that even under lower deposition potential, we still observe the dominant peak of Cu on S edges (Fig. 4). Based on these data, further operando XAS measurements would be needed to investigate Cu UPD on TMDs in more detail.<sup>26</sup>

#### Critical evaluation of Cu UPD to determine $N_{\text{AS}}$ of TMDs.—

Recently, the Cu UPD method has been used to measure the number of HER active sites on WS<sub>2</sub>, MoS<sub>2</sub> and Pd<sub>3</sub>P<sub>2</sub>S<sub>8</sub>.<sup>22–24</sup> However, whether Cu adsorbs on the same sites, where hydrogen evolution happens, remains an unresolved question. Particularly as shown in Fig. 1, there is no clear H UPD region in MoS<sub>2</sub> and WS<sub>2</sub> making it impossible to derive  $Q_{\text{H}}$ . Nevertheless, the Cu UPD charge ( $Q_{\text{Cu}}$ ) and hydrogen adsorption charge (“ $Q_{\text{H}}$ ”) were compared and adopted in TMDs-based electrocatalysts.<sup>22–24</sup> Here, we use the background capacitive charge ( $Q_{\text{BC}}$ ) as a background correction to determine the charge which goes to the Cu UPD process ( $Q_{\text{Cu}}$ ). To correlate the relative  $Q_{\text{Cu}}$  with  $Q_{\text{BC}}$ , a plot of  $Q_{\text{Cu}}/Q_{\text{BC}}$  as a function of deposition

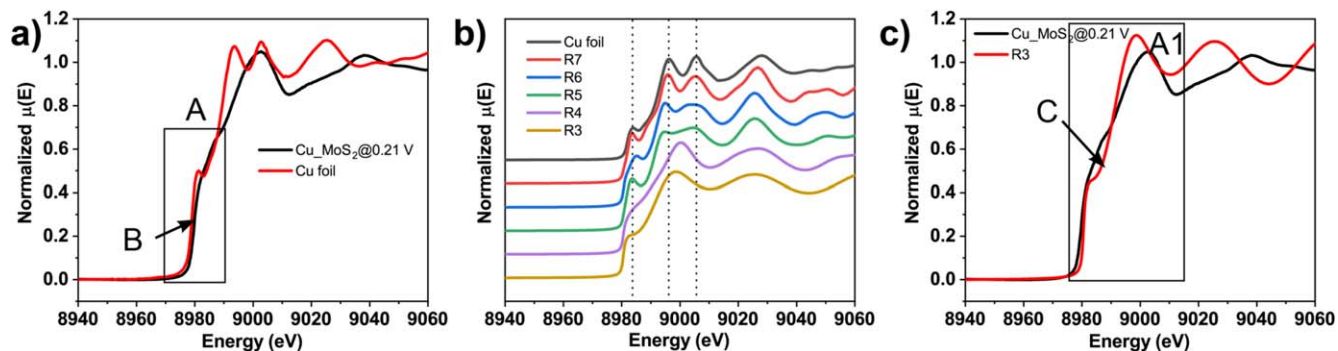


**Figure 3.** (a) XANES spectra for Cu\_MoS<sub>2</sub>@0.21 V (black curve) and Cu foil (red curve), label “A” indicates the spectral region in the rectangular box and label “B” indicates the spectra shift; (b) theoretical model of XANES system revealed particle size induced progressive changing in XANES features for metallic Cu, and the smallest particle used for the modeling possessed a cluster size of 3.0 Å (R3) containing 12 Cu; (c) XANES spectra of Cu\_MoS<sub>2</sub>@0.21 V and R3, region “A1” represents the spectra in the rectangular region and label “C” indicates the shoulder feature.

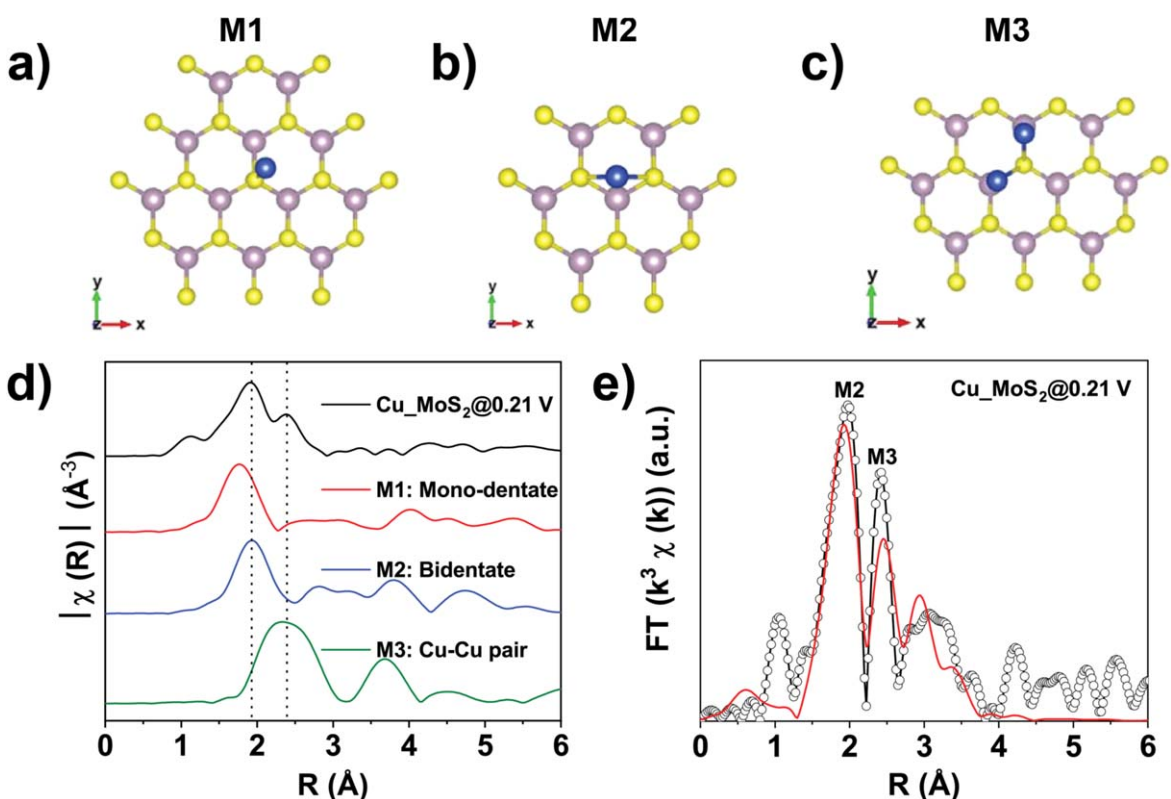


**Figure 4.** Structural models of Cu bonding on MoS<sub>2</sub> with configurations of Cu monodentate (a), bidentate binuclear (b) and paired Cu monodentate (c); (d) comparison of experimental (black curve) and FEFF modeled EXAFS magnitude of Fourier Transforms (FT); (e) fitted results corresponding to the Cu K-edge EXAFS magnitude of FT spectra. Data are plotted as open circles and fits as red line.

potential is presented in Fig. 5a.<sup>8</sup>  $Q_{Cu}$  is obtained by integrating the Cu stripping charge from the Cu deposition potential ( $E_{Dep}$ ) to +0.67 V vs RHE (corrected for MoS<sub>2</sub> background  $Q_{BC}$  in 0.1 M H<sub>2</sub>SO<sub>4</sub>), whereas  $Q_{BC}$  is calculated with the same method in the absence of CuSO<sub>4</sub>. The  $Q_{Cu}/Q_{BC}$  ratio reaches a value of  $\sim 2$  in a narrow potential window of +0.44–0.46 V vs RHE for MoS<sub>2</sub> (Fig. 5a, Table SI) and WS<sub>2</sub> (Fig. 5b, Table SII). However, we should point out that  $Q_{Cu}/Q_{BC}$  ratio of  $\sim 2$  does not necessarily suggest the same surface density between copper and hydrogen atoms under such conditions.<sup>22,23</sup> First of all, the absence of a clear H UPD signature in MoS<sub>2</sub> and WS<sub>2</sub> leads to a unknown quantitative relation between Cu UPD and H UPD sites making a quantitative evaluation of H adsorption sites via the Cu UPD method impossible. Secondly, other factors such as (i) different accessibility of solvated Cu<sup>2+</sup> to nanostructured TMD sites compared to H<sup>+</sup>, (ii) Cu cluster formation due to the improper selection of the  $E_{dep}$  window and scan

rate, (iii) variations in crystallinity of TMD leading to presence of different HER active sites, and (iv) difference in nature of HER and Cu UPD sites such as basal plane adsorption of Cu on TMDs, can also influence the validity of Cu UPD method and are difficult to control. All these above aspects imply that the direct transfer of the Cu UPD method from noble metal systems with a clear H UPD phenomenon to TMDs appears to be not appropriate.

In order to further evaluate the applicability of the Cu UPD method in relatively comparing different samples based on the number of active sites for the electrocatalytic HER, we measured  $Q_{Cu}$ , the double layer capacitance ( $C_{dl}$ ) and the HER current density at –0.4 and –0.6 V vs RHE for a selection of MoS<sub>2</sub> (Figs. 5c, 5d) and WS<sub>2</sub> (Figs. 5e, 5f) samples; see Table SIII for sample IDs and preparation details. The linear sweep voltammetry (LSV) curves of different WS<sub>2</sub> and MoS<sub>2</sub> films are presented in Fig. S2, S6 and the current density values at certain overpotentials presented in Fig. 5

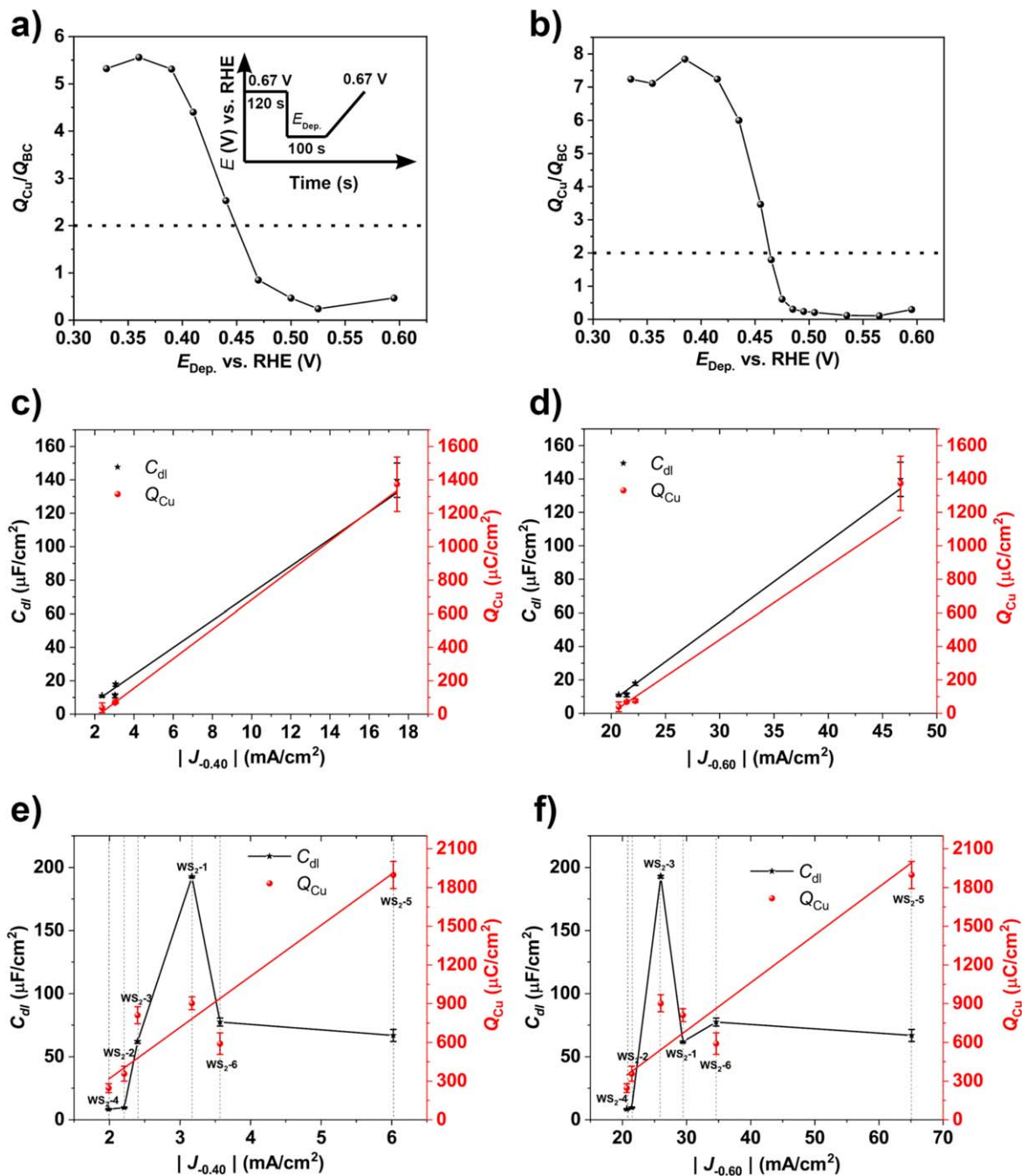


**Figure 5.** (a) Ratio of Cu stripping charge to background charge as a function of adsorption potential on nanostructured MoS<sub>2</sub> in 2 mM CuSO<sub>4</sub> in 0.1 M H<sub>2</sub>SO<sub>4</sub>. Inset shows the Cu stripping process where MoS<sub>2</sub> is first polarized at +0.67 V vs RHE for 120 s, then after Cu deposition at certain potential  $E_{Dep.}$  for 100 s, the Cu is stripped by scanning back to +0.67 V at a scan rate of 2 mV s<sup>-1</sup>. (b) ratio of Cu stripping charge to background hydrogen adsorption charge as a function of adsorption potentials on WS<sub>2</sub> film. (c)–(f) Plots of current density values of a selection of MoS<sub>2</sub> (c), (d) a WS<sub>2</sub> (e), (f) samples at –0.40 V and –0.60 V vs RHE vs double layer capacitance ( $C_{dl}$ ) (black) and Cu stripping charge ( $Q_{Cu}$ ) (red).

reflect their HER performance.  $Q_{Cu}$  is calculated by integrating the CV curve of the samples in 2 mM CuSO<sub>4</sub> in 0.1 M H<sub>2</sub>SO<sub>4</sub> from +0.46 to +0.67 V vs RHE corrected for the background charge. The double layer capacitance ( $C_{dl}$ ) was extracted by plotting  $\Delta j = j_a - j_c$  ( $j_a$  and  $j_c$  represent anodic and cathodic current densities, respectively) at a given potential against CV scan rates using the following equation:  $\frac{j_a - j_c}{2} = C_{dl} \frac{dE}{dt}$  (Fig. S3). Current densities at both –0.40 and –0.60 V show that WS<sub>2</sub>-5 presents the highest current density value. However,  $C_{dl}$  measurements show a significantly higher value for WS<sub>2</sub>-1 compared to the other WS<sub>2</sub> films which clearly does not correlate with their HER activities. Therefore, evaluating the ECSA with  $C_{dl}$  in this case would lead to a random correlation with HER

activity.<sup>19,45</sup> In contrast,  $Q_{Cu}$  values shown in Fig. 5e, f display the same trend as HER activity at both –0.40 and –0.60 V vs RHE, which suggests that Cu UPD apparently better correlates with HER activity and therefore would be a more reliable method for the determination of ECSA than  $C_{dl}$ . The correlation of Cu UPD ( $Q_{Cu}$ ) with HER activity of MoS<sub>2</sub> films is shown in Figs. 5c, 5d. With Cu UPD we can assess the number of Cu UPD adsorption sites which apparently relates linearly to the HER activity of the tested samples allowing a relative comparison of  $N_{AS}$  (Tables I, II). A quantitative relation between  $N_{Cu\ UPD}$  sites and  $N_{AS}$  (HER) cannot be easily established due to the absence of the H UPD phenomenon on the tested nanostructured TMD samples. Further experiments, e.g.

**Table I. Summary of calculated adsorbed Cu based on the integration of Cu stripping in the range of 0.46–0.67 V vs RHE shown in Fig. S5.**

Sample name	$N_{AS}$ (amount of adsorbed Cu) $\text{cm}^{-2}$
WS <sub>2</sub> -1	$2.8 \times 10^{15}$
WS <sub>2</sub> -2	$1.1 \times 10^{15}$
WS <sub>2</sub> -3	$2.5 \times 10^{15}$
WS <sub>2</sub> -4	$7.7 \times 10^{14}$
WS <sub>2</sub> -5	$5.9 \times 10^{15}$
WS <sub>2</sub> -6	$1.8 \times 10^{15}$

**Table II. Summary of calculated adsorbed Cu based on the integration of Cu stripping in the range of 0.46–0.67 V vs RHE shown in Fig. S9.**

Sample name	$N_{AS}$ (amount of adsorbed Cu) $\text{cm}^{-2}$
MoS <sub>2</sub> -1	$1.2 \times 10^{14}$
MoS <sub>2</sub> -2	$2.2 \times 10^{14}$
MoS <sub>2</sub> -3	$2.4 \times 10^{14}$
MoS <sub>2</sub> -4	$4.4 \times 10^{15}$

in situ scanning tunneling microscopy (STM) on single crystal MoS<sub>2</sub> and WS<sub>2</sub> model samples, would be needed to create a more solid link between  $N_{Cu\ UPD}$  sites and  $N_{AS}$  (HER). Importantly, parameters such as deposition potential window and porosity of the catalysts should be considered when using Cu UPD as a method for ECSA estimation. With that, the relation between  $N_{Cu\ UPD}$  sites and  $N_{AS}$  (HER) can be presented as  $N_{AS}$  (HER) =  $a * N_{Cu\ UPD} + b$  with  $a$  being a constant between 0 and 1 and  $b$  being a constant considering the Cu deposition on basal planes of TMDs and/or Cu cluster formation.

## Conclusions












Underpotential deposition of copper on MoS<sub>2</sub> and WS<sub>2</sub> is investigated. EQCM has been used to show the adsorption of Cu atoms on TMDs under underpotential deposition conditions. The bonding structure of adsorbed Cu on MoS<sub>2</sub> has been characterized by *ex situ* grazing incidence XAS in comparison with DFT models, showing a bidentate binuclear bonding on MoS<sub>2</sub> basal planes. Compared to double layer capacitance measurements, Cu UPD demonstrates a better apparent correlation with HER activity and therefore would allow a more reliable evaluation of the number of HER active sites in TMDs. However, the formation of Cu clusters cannot be avoided with regard to a more negative (compared to Nernst Cu deposition potential) deposition potential range. Furthermore, due to the absence of H UPD, the correlation between Cu deposition sites—where basal plane adsorption cannot be excluded—and HER active sites (edge sites) needs to be further validated via *in situ* electrochemical STEM or XAS. Due to the complexity of the TMDs and the specific nature of their HER active sites (i.e. edge sites), a direct comparison with the Cu UPD phenomenon on noble metals such as Pt is not possible. A quantitative ECSA determination in TMDs requires edge site selective probes, such as used in NO titration FTIR spectroscopy as applied in our previous work.<sup>46</sup>

## Acknowledgments

This work is part of the program “CO<sub>2</sub>-neutral fuels” (project 13-CO26) of the Foundation for Fundamental Research on Matter (FOM), which was financially supported by the Netherlands Organization for Scientific Research (NWO). This research program was co-financed by Shell Global Solutions International B.V. N.Y. Dzade acknowledges the UK Engineering and Physical Sciences

Research Council (EPSRC) for funding (grant No. EP/S001395/1). This work also made use of the facilities of ARCHER (<http://archer.ac.uk>), the UK’s national supercomputing service via the membership of the UK’s HEC Materials Chemistry Consortium, which is funded by EPSRC (EP/L000202). S. Balasubramanyam, A. Sharma and A. Bol acknowledge financial support from the European Research Council (grant Agreement No.648787-ALDof2DTMDs).

## ORCID

Longfei Wu  <https://orcid.org/0000-0001-6330-3613>  
 Nelson Y. Dzade  <https://orcid.org/0000-0001-7733-9473>  
 Ning Chen  <https://orcid.org/0000-0002-1269-6119>  
 Shashank Balasubramanyam  <https://orcid.org/0000-0001-8728-9780>  
 Akhil Sharma  <https://orcid.org/0000-0003-1837-3262>  
 Lu Gao  <https://orcid.org/0000-0002-7127-9980>  
 Dennis G. H. Hetterscheid  <https://orcid.org/0000-0001-5640-4416>  
 Emiel J. M. Hensen  <https://orcid.org/0000-0002-9754-2417>  
 Ageeth A. Bol  <https://orcid.org/0000-0002-1259-6265>  
 Nora H. De Leeuw  <https://orcid.org/0000-0002-8271-0545>  
 Jan P. Hofmann  <https://orcid.org/0000-0002-5765-1096>

## References

1. S. Trasatti and O. A. Petrii, *Pure & Appl. Chem.*, **63**, 711 (1991).
2. G. Kokkinidis, *J. Electroanal. Chem.*, **201**, 217 (1986).
3. S. Trasatti and O. A. Petrii, *J. Electroanal. Chem.*, **327**, 353 (1992).
4. J. Clavilier, K. El Achi, M. Petit, A. Rodes, and M. A. Zamakhchari, *J. Electroanal. Chem.*, **295**, 333 (1990).
5. J. Zhang and J. Math, *Anal. Appl.*, **328**, 220 (2007).
6. M. L. Personick, M. R. Langille, J. Zhang, and C. A. Mirkin, *Nano Lett.*, **11**, 3394 (2011).
7. G. Herzog and D. W. M. Arrigan, *TrAC Trends in Anal. Chem.*, **24**, 208 (2005).
8. C. L. Green and A. Kucernak, *J. Phys. Chem. B*, **106**, 1036 (2002).
9. A. S. Bakavets, Y. M. Aniskevich, G. A. Ragoisha, and E. A. Streltsov, *Electrochem. Commun.*, **94**, 23 (2018).
10. Q. Ding, B. Song, P. Xu, and S. Jin, *Chem.*, **1**, 699 (2016).
11. J. D. Benck, T. R. Hellstern, J. Kibsgaard, P. Chakthranont, and T. F. Jaramillo, *ACS Catal.*, **4**, 3957 (2014).
12. Y. Hou, X. Zhuang, and X. Feng, *Small Methods*, **1**, 1700090 (2017).
13. L. Wu, A. J. F. van Hoof, N. Y. Dzade, L. Gao, M. I. Richard, H. Friedrich, N. H. De Leeuw, E. J. M. Hensen, and J. P. Hofmann, *Phys. Chem. Chem. Phys.*, **21**, 6071 (2019).
14. K. S. W. Sing, D. H. Everrett, R. A. W. Haul, L. Moscou, R. A. Pierotti, J. Rouquérol, and T. Siemieniowska, *Pure & Appl. Chem.*, **57**, 603 (1985).
15. J. Kibsgaard, C. Tsai, K. Chan, J. D. Benck, J. K. Norskov, F. Abild-Pedersen, and T. F. Jaramillo, *Energy Environ. Sci.*, **8**, 3022 (2015).
16. Y. Zhang, L. Gao, E. J. M. Hensen, and J. P. Hofmann, *ACS Energy Lett.*, **3**, 1360 (2018).
17. S. Li, G. Zhang, X. Tu, and J. Li, *ChemElectroChem*, **5**, 701 (2018).
18. M. Łukaszewski, M. Soszko, and A. Czerwiński, *Int. J. Electrochem. Sci.*, **11**, 4442 (2016).
19. Y. Yoon, B. Yan, and Y. Surendranath, *J. Am. Chem. Soc.*, **140**, 2397 (2018).
20. D. Voiry, M. Chhowalla, Y. Gogotsi, N. A. Kotov, Y. Li, R. M. Penner, R. E. Schaak, and P. S. Weiss, *ACS Nano*, **12**, 9635 (2018).
21. Y. M. Aniskevich, M. V. Malashchona, P. V. Chulkin, G. A. Ragoisha, and E. A. Streltsov, *Electrochim. Acta*, **220**, 493 (2016).
22. D. Voiry et al., *Nat. Mater.*, **12**, 850 (2013).
23. X. Zhang et al., *Nat. Catal.*, **1**, 460 (2018).
24. S. Balasubramanyam, M. Shirazi, M. A. Bloodgood, L. Wu, M. A. Verheijen, V. Vandalon, W. M. M. Kessels, J. P. Hofmann, and A. A. Bol, *Chem. Mater.*, **31**, 5104 (2019).
25. A. Sharma, M. A. A. Verheijen, L. Wu, S. Karwal, V. Vandalon, H. C. M. Knoop, R. S. Sundaram, J. P. Hofmann, W. M. M. Kessels, and A. A. Bol, *Nanoscale*, **10**, 8615 (2018).
26. L. Wu, A. Longo, N. Y. Dzade, A. Sharma, M. Hendrix, A. A. Bol, N. H. de Leeuw, E. J. M. Hensen, and J. P. Hofmann, *ChemSusChem*, **12**, 4383 (2019).
27. D. Cabaret, Y. Joly, H. Renevier, and C. R. Natoli, *J. Synchrotron Rad.*, **6**, 258 (1999).
28. K. Lejaeghere, V. Van Speybroeck, G. Van Oost, and S. Cottenier, *Crit. Rev. Solid State Mater. Sci.*, **39**, 1 (2013).
29. G. Kresse and J. Furthmüller, *J. Comput. Mat. Sci.*, **6**, 15 (1996).
30. G. Kresse and J. Hafner, *Phys. Rev. B*, **47**, 558 (1993).
31. P. E. Blöchl, *Phys. Rev. B*, **50**, 17953 (1994).
32. J. P. Perdew, K. Burke, and M. Ernzerhof, *Phys. Rev. Lett.*, **77**, 3865 (1996).
33. S. Grimme, J. Antony, S. Ehrlich, and H. Krieg, *J. Chem. Phys.*, **132**, 154104 (2010).
34. Y. Jung, Y. Zhou, and J. J. Cha, *Inorg. Chem. Front.*, **3**, 452 (2016).
35. N. Onofrio, D. Guzman, and A. Strachan, *J. Chem. Phys.*, **145**, 194702 (2016).
36. H. Uchida, M. Hiei, and M. Watanabe, *J. Electroanal. Chem.*, **452**, 97 (1998).

37. G. L. Borges, K. K. Kanazawa, and J. G. Gordon II, *J. Electroanal. Chem.*, **364**, 281 (1994).
38. F. Gloaguen, J.-M. Léger, and C. Lamy, *J. Electroanal. Chem.*, **467**, 186 (1999).
39. M. R. Deakin and O. Melroy, *J. Electroanal. Chem.*, **239**, 321 (1988).
40. D. G. H. Hetterscheid, *Chem Commun (Camb)*, **53**, 10622 (2017).
41. H. S. Yee and H. D. Abruña, *J. Phys. Chem.*, **97**, 6278 (1993).
42. S. W. Price, J. D. Speed, P. Kannan, and A. E. Russell, *J. Am. Chem. Soc.*, **133**, 19448 (2011).
43. T. F. Jaramillo, K. P. Jørgensen, J. Bonde, J. H. Nielsen, S. Horch, and I. Chorkendorff, *Science*, **317**, 100 (2007).
44. C. Tsai, H. Li, S. Park, J. Park, H. S. Han, J. K. Nørskov, X. Zheng, and F. Abild-Pedersen, *Nature Commun.*, **8**, 15113 (2017).
45. S. Watzel and A. S. Bandarenka, *Electroanalysis*, **28**, 2394 (2016).
46. L. Wu, N. Y. Dzade, M. Yu, B. Mezari, A. J. F. van Hoof, H. Friedrich, N. H. de Leeuw, E. J. M. Hensen, and J. P. Hofmann, *ACS Energy Lett.*, **4**, 1733 (2019).